Revisiting Antlia 2's Effect on the Outer Disk

Tetsuto Nagashima[a,b], Sukanya Chakrabarti[c], Peter Craig[c]

[a] *Institute for Astronomy, University of Hawai'i, 2680 Woodlawn Drive, Honolulu, HI 96822, USA*

[b] *Department of Physics and Astronomy, University of Southern California, Los Angeles, CA, 90089, USA*

[c] *School of Physics and Astronomy, Rochester Institute of Technology, 84 Lomb Memorial Dr., Rochester, NY 14623, USA*

Abstract

Antlia 2 is the lowest surface-brightness satellite galaxy to our Milky Way that was discovered using data by the Gaia Mission, in the second data release (DR-2). Previous publications suggest that Antlia 2 may be responsible for observed large perturbations in the outer HI disk of our Galaxy. Earlier calculations used Gaia DR-2 proper motion measurements to constrain the stars within Antlia 2 and determine its orbit. It was found that low pericenter orbits (∼10 kpc) produce disturbances that match the observed perturbations. We use newly calculated Gaia EDR3 proper motions of Antlia 2 to compute pericenter distributions. We also independently recalculate the Gaia EDR3 proper motions of Antlia 2 using our own selection criteria and compare it to the range needed to produce the requisite low pericenter orbits. Since Gaia EDR3 has significantly less error, our results should be less sensitive to selection criteria. By exploring how this updated proper motion calculations affect the orbit, we can reevaluate Antlia 2's dynamical effect on the gas disk of the Milky Way.

Keywords: Antlia 2, Galactic dynamics

1. Introduction

The interactions between the Milky Way and nearby dwarf galaxies are crucial to understanding the formation and structure of the universe. The Λ Cold Dark Matter (ΛCDM) model predicts that galaxies like the Milky Way form through a series of merging and accretion events involving smaller systems. Based on this hierarchical cosmological model, the Milky Way should have accreted $\sim 100-200$ satellite galaxies from the past 12 Gyr (Bullock and Johnston, 2005). Galaxy formation processes are simulated with distinctions between the evolution of visible and dark matter in these satellites, which is essential to modeling a stellar halo that is similar to that of the Milky Way and matches its observed number

Email address: `tetsnaga@usc.edu` (Tetsuto Nagashima)

of surviving satellites. Stars in the inner halo, outer halo, and stars that were affected by disruption events are all expected to have different chemical compositions, so understanding how and what the Milky Way interacted with in the past can refine our hierarchical model of cosmology (Bullock and Johnston, 2005).

The outer Galaxy is in particular an ideal environment for studying dwarf galaxy interactions. Large perturbations in the outer Galaxy can be more cleanly attributed to external perturbers (for regions beyond the stellar disk). The outer HI disks of galaxies are colder than the stars (and therefore more responsive to perturbations), are more extended than the stellar disk, and thereby can act as an effective calorimeter for gravitational interactions (Chakrabarti and Blitz, 2009). A detailed map of the surface density of neutral hydrogen in the Milky Way revealed perturbations in the outer disk (Levine et al., 2006). These perturbations could not be produced in a purely isolated context; earlier work found that the observed HI disturbances could be caused by a dark sub-halo that tidally interacted with the Milky Way disk (Chakrabarti and Blitz, 2009). This perturber was estimated to have a 1:100 mass ratio with orbital pericenter ~ 10 kpc (Chakrabarti and Blitz, 2009) at a current radial distance of ~ 130 kpc.

The *Gaia* satellite has produced a wealth of data on the Milky Way. The release of *Gaia* DR-2 gave access to high quality proper motion measurements which were used to discover the Antlia 2 dwarf galaxy (Torrealba et al., 2019). Antlia 2 was dubbed a "hidden giant" because although it has a similar half-light radius as the Large Magellanic Cloud, it is about 4000 times fainter. Its location at a low galactic latitude behind the Milky Way's central disk coupled with its dim aspect are likely responsible for it not having been detected in previous surveys. Intriguingly, the ΛCDM model proposes that dark matter sub-halos often contain very dim dwarf galaxies, and Antlia 2 is at a radial location that matched previous predictions of where a dwarf galaxy drove ripples in the outer disk (Chakrabarti and Blitz, 2009). Furthermore, the orbit of Antlia 2 is nearly coplanar to the Galactic disk. If Antlia 2 was responsible for the perturbations in the outer disk, its proper motions would be constrained to those that would give a lower pericenter (Chakrabarti et al., 2019). Using *Gaia* EDR3, we will obtain proper motion calculations with lower error and reexamine Antlia 2's orbital distribution and pericenters to compare them to those predicted in Chakrabarti et al. (2019).

2. Method

To ensure that our methods are robust across both data releases, we reproduce the orbital distributions using DR-2 proper motion calculations (Torrealba et al., 2019) (Chakrabarti et al., 2019). Next, we incorporate the EDR3 proper motions calculated by McConnachie and Venn (2020) to compare results across data releases.

Once we have the location and proper motions of the center of Antlia 2, these three-dimensional positions and velocities are used as initial conditions for the equation of motion (Besla et al., 2007). We take into account the gravitational potential of the Milky Way and the dynamical friction due to the passage of Antlia 2 through the dark matter halo of the Milky Way:

$$\ddot{\mathbf{r}} = \frac{\partial}{\partial \mathbf{r}} \phi_{MW}(|\mathbf{r}|) + \frac{\mathbf{F}_{DF}}{M_{SAT}} \tag{1}$$

where ϕ_{MW} is the gravitational potential of the Milky Way, $\mathbf{r}$ is the position vector of Antlia 2 with respect to the galactic center, $\mathbf{F}_{DF}$ is the dynamical friction term, and M_{SAT} is the mass of Antlia 2.

To consider the orbit of Antlia 2, we must infer its mass. There exists a relationships between the stellar mass and stellar metallicity of galaxies; higher-mass galaxies are better at retaining their metals, while lower-mass galaxies lack the gravitational influence to prevent losing their metals to supernova winds, stellar winds, and galaxy-scale feedback. Based on DR-2 data, Antlia 2 was reported to have a mean metallicity [Fe/H] = -1.39 (Torrealba et al., 2019), which by the mass-metallicity relation (Kirby et al., 2013) should correspond to a stellar mass of $\sim 10^7 M_\odot$. Then, a relationship between star formation rate and a satellite galaxy's pre-infall halo mass (Read and Erkal, 2019) was used to derive halo mass from stellar mass. The satellite mass of Antlia 2 was inferred to be $10^{10} M_\odot$ (Chakrabarti et al., 2019). However, a more recent analysis claims this metallicity was an overestimate, with the updated metallicity of Antlia 2 at $[Fe/H] = -1.77$ (Ji et al., 2021). This newly reported metallicity corresponds to a substantially smaller satellite mass of Antlia 2, so in Figure 1 we use the original satellite mass $10^{10} M_\odot$ reported in Chakrabarti et al. (2019) and compare it to orbits with smaller satellite masses that would correspond to lower metallicities.

It is important to consider the satellite mass of Antlia 2 because of how it affects our calculation of the drag force to due dynamical friction. Dynamical friction (DF) occurs when moving bodies gravitationally interact with surrounding matter in space and lose momentum and energy. A massive object like Antlia 2 moves through particles and attracts them towards itself. As the object continues moving, the particles are more densely concentrated behind the object than in front, which results in a net drag force. The dynamical friction force is proportional to the square of the satellite mass Besla et al. (2007), so a smaller object loses less energy to friction and travels through a lower apocenter orbit.

This can be seen in Figure 1 where the McConnachie and Venn (2020) proper motion measurements of Antlia 2 are integrated in four cases: (a) without dynamical friction, (b) including dynamical friction with satellite mass $M_{SAT} = 1 \times 10^9 M_\odot$, (c) $M_{SAT} = 3 \times 10^9 M_\odot$, (d) $M_{SAT} = 5 \times 10^9 M_\odot$, and the earlier inferred Antlia 2 mass $M_{SAT} = 1 \times 10^{10} M_\odot$ (Chakrabarti et al., 2019). We select these masses to compare the original satellite mass $10^{10} M_\odot$ reported in Chakrabarti et al. (2019) and the a few smaller satellite masses that would correspond to updated lower metallicities. As expected, the orbit not accounting for dynamical friction has the lowest apocenter orbit and apocenter increases with satellite mass.

To solve the equation of motion, we select a Milky Way potential ϕ_{MW} and numerically

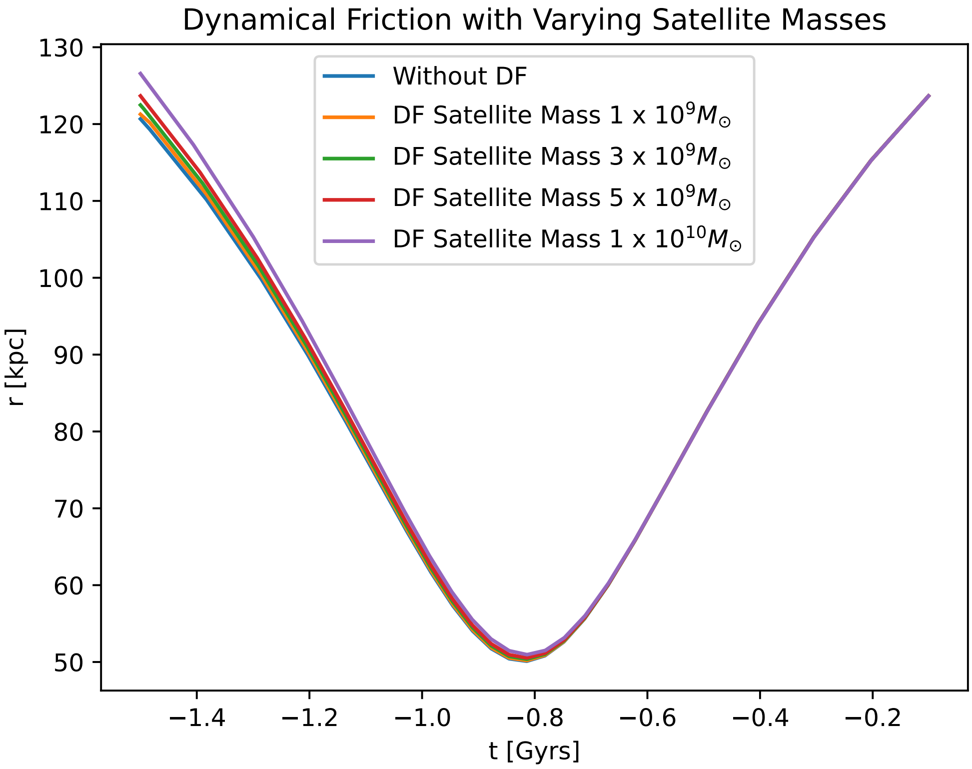

Figure 1: Radial distance from the center of the Milky Way plotted as a function of time. Orbital integrations were calculated in a matched Hernquist potential highlighting the effect of dynamical friction (DF) with varying satellite masses. A more massive satellite loses more energy to dynamical friction, which means it came from an orbit with a higher apocenter.

integrate backwards in time to solve for the orbits using an 8th order Runge-Kutta method (Chang and Chakrabarti, 2011).

The Milky Way potential depends on the mass distribution of dark matter throughout the galaxy. We assume that the dark matter halo of the Milky Way is static and spherically symmetric. The Hernquist (1990) and Navarro et al. (1997) (NFW) profiles model the dark matter distribution in the galaxy as a function of radius. The Hernquist profile is given by

$$\rho_{Hern}(r) = \frac{M}{2\pi}\frac{a}{r(r+a)^3}, \tag{2}$$

where a is the scale radius. The NFW profile slightly differs from Hernquist, i.e.

$$\rho_{NFW}(r) = \frac{\rho_0}{\frac{r}{r_s}(1+\frac{r}{r_s})^2} \tag{3}$$

where ρ_0 is the critical density and r_s is the NFW scale length

We match the Hernquist profile to the NFW profile in the inner regions as in Springel et al. (2005) by setting the total mass of the Hernquist profile equal to the mass contained within the virial radius r_{200} of an NFW-halo and the densities equal to each other for $r \ll r_{200}$. To do so, we relate the NFW concentration index c = r_{200}/r_s to the Hernquist scale radius a:

$$a = r_s\sqrt{2[ln(1+c) - c/(1+c)]} \tag{4}$$

For large r, the NFW profile drops off at $\rho_{NFW} \propto r^{-3}$, while the Hernquist profile drops off at $\rho_{Hern} \propto r^{-4}$. Unlike the NFW profile, the total mass of the Hernquist profile converges, allowing us to model isolated halos without truncating the distribution. Since varying the total mass of the distribution will significantly affect a satellite's orbit, we reproduced the plots for orbital distributions and their mass dependence in Chakrabarti et al. (2019) with Gaia DR-2 data. Assuming the system of Antlia 2 and the Milky Way satisfies the virial theorem, we refer to the relationship between virial mass, velocity, and radius given in Springel and White (1999):

$${v_{200}}^2 = \sqrt{\frac{GM_{200}}{R_{200}}} \tag{5}$$

Higher values of v_{200} correspond with higher masses M_{200}, and a higher Milky Way mass means the satellite is more tightly bound, so the calculated orbits should have lower pericenters.

We performed the integration with various virial velocities ranging from v_{200} = 160 km/s, 180 km/s, and 200 km/s. This is corresponding to virial masses $M_{200} = 1.24 \times 10^{12} M_\odot$, $1.57 \times 10^{12} M_\odot$, and $1.93 \times 10^{12} M_\odot$, which is consistent with expectations from the literature (Chakrabarti et al., 2019). We took 1000 proper motion samples from a normal distribution based on the mean and standard deviation of the proper motion of Antlia 2. To recreate the

Table 1: Mean EDR3 pericenters for orbital integrations in various density profiles, Milky Way masses, and dynamical friction considerations. Hernquist-NFW denotes the matched Hernquist profile while NFW denotes a pure NFW density profile.

Density Profile	Dynamical Friction?	v_{200} [km/s]	M_{200} [$M_\odot$]	R_p [kpc]
Hernquist-NFW	N	160	1.24×10^{12}	50.3 ± 4.3
Hernquist-NFW	Y	160	1.24×10^{12}	51.4 ± 4.3
Hernquist-NFW	N	180	1.57×10^{12}	41.8 ± 3.4
Hernquist-NFW	Y	180	1.57×10^{12}	42.7 ± 3.4
Hernquist-NFW	N	200	1.93×10^{12}	35.5 ± 2.7
Hernquist-NFW	Y	200	1.93×10^{12}	36.2 ± 2.9
Pure NFW	N	160	1.24×10^{12}	57.2 ± 4.6
Pure NFW	Y	160	1.24×10^{12}	58.6 ± 4.7
Pure NFW	N	180	1.57×10^{12}	48.0 ± 3.8
Pure NFW	Y	180	1.57×10^{12}	48.8 ± 3.9
Pure NFW	N	200	1.93×10^{12}	41.0 ± 3.1
Pure NFW	Y	200	1.93×10^{12}	41.8 ± 3.2

results from *Gaia* DR-2, we used both the proper motions given in Torrealba et al. (2019) and Chakrabarti et al. (2019) and backward integrating the orbits in the matched Hernquist potential to create histograms of the pericenter distributions.

We then used Gaia EDR3 proper motion measurements of Antlia 2 as reported recently in (McConnachie and Venn, 2020) and produced the pericenter distributions. Since these proper motion measurements are more accurate than those from DR-2, their corresponding distributions should have lower standard deviations.

3. Results and Discussion

We proceed to using *Gaia* EDR3 proper motions of Antlia 2 calculated by McConnachie and Venn (2020). We sampled 1000 proper motions from a normal distribution based on the mean and standard deviation of the proper motion measurements, then integrated all of them to create pericenter distributions. We repeated this for various density profiles and dynamical friction considerations for virial velocities v_{200} = 160 - 200 km/s.

Table 1 lists the mean pericenters for these orbital integrations. As expected, higher virial velocities correspond to lower mean pericenters and the distributions using EDR3 data have lower standard deviations.

We also overlay the pericenter distributions to compare the results across density profiles and dynamical friction considerations. Figures 2 and 3 are pericenter distributions in a matched Hernquist profile without dynamical friction, a Hernquist profile with dynamical friction, and a pure NFW profile without dynamical friction. Figure 2 is based on DR-2 proper motions (Chakrabarti et al., 2019) while Figure 3 uses EDR3 proper motions (McConnachie and Venn, 2020). Clearly, the DR-2 distributions are wider, indicating that more accurate EDR3 proper motion measurements have given us a more accurate picture of the orbit of Antlia 2. It is also worth noting that the EDR3 distributions are significantly higher than those derived from DR-2 calculations.

For cases involving dynamical friction, the satellite mass was set to $10^{10} M_{\odot}$, the mass of Antlia 2 reported in Chakrabarti et al. (2019). For all integrations in Table 1, accounting for dynamical friction did not make a significant difference in mean pericenter. This aligns with our expectations since accounting for dynamical friction should have a larger effect on the apocenter of the orbit. Using the pure NFW profile instead of the matched Hernquist profile seems to result in slightly higher pericenters, but the difference is not significant.

4. Conclusions

The large planar disturbances in the outer HI disk of our Galaxy (Levine et al., 2006) have been a long-standing puzzle. Earlier dynamical analysis found that they could be produced by a massive dwarf galaxy on a close approach (Chakrabarti and Blitz, 2009). The recent discovery of the Antlia 2 dwarf galaxy from Gaia DR-2 (Torrealba et al., 2019) was a compelling candidate (Chakrabarti et al., 2019) to explain these disturbances. Motivated by the release of Gaia EDR3, we revisited the earlier analysis of the DR-2 data (for which the proper motions had substantially larger error bars) by Chakrabarti et al. (2019). We have checked that we recover the prior results for the pericenter distributions using DR-2 proper motion calculations from Torrealba et al. (2019) and Chakrabarti et al. (2019). As expected, the EDR3 proper motions are much more precise than DR-2, and here we have used orbit integration calculations to find that the the EDR3 proper motions (McConnachie and Venn, 2020) imply larger pericenters on average relative to DR-2. Recent work (Ji et al., 2021) indicates that the discovery paper on Antlia 2 (Torrealba et al., 2019) overestimated the metallicity of Antlia 2, which would suggest a lower progenitor mass for Antlia 2 than was considered earlier (Chakrabarti et al., 2019).

At face value, these newer results seem to suggest that Antlia 2 may not be the long-sought after culprit to explain the disturbances in the outer HI disk. However, our orbit integration calculations here did not include the effect of the LMC. Recent work (Ji et al., 2021) suggests that (even within an approximate framework) including the effect of the reflex motion of the LMC will produce lower pericenters for Antlia 2 that agree more closely with previous results. The potentials that we have considered here are spherically symmetric and the inclusion of a disk potential can also be expected to increase the tidal effect. More fundamentally, the HI map produced by Levine et al. (2006) *assumed* kinematic distances. It will be interesting to see whether a more accurate HI map produced using asteroseismic distances (Auge et al., 2020) will still yield large planar disturbances as in the original HI map constructed by Levine et al. (2006).

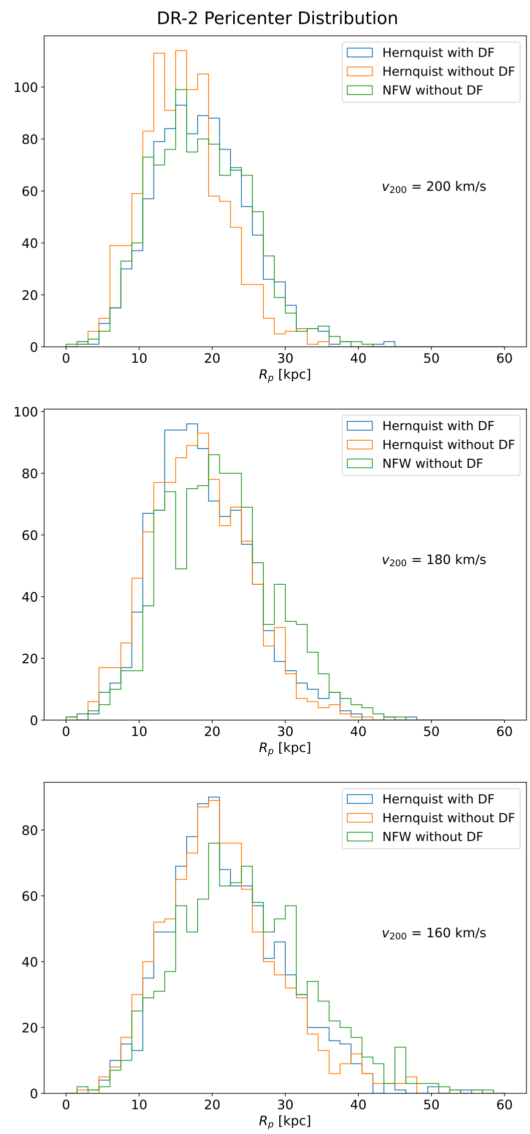

Figure 2: Pericenter distributions using 1000 samples from proper motion calculations made by Chakrabarti et al. (2019) with varying virial masses. Orbits were integrated in a matched Hernquist potential with dynamical friction, a matched Hernquist potential without dynamical friction, and a pure NFW potential without dynamical friction. The step histograms were plotted together to compare the effects on pericenter distributions. Compared to the matched Hernquist profile without dynamical friction (orange), the NFW profile (green) results in slightly higher pericenters within error bars. Taking into account for dynamical friction (blue) results in slightly lower mean pericenters, but the effect is not significant.

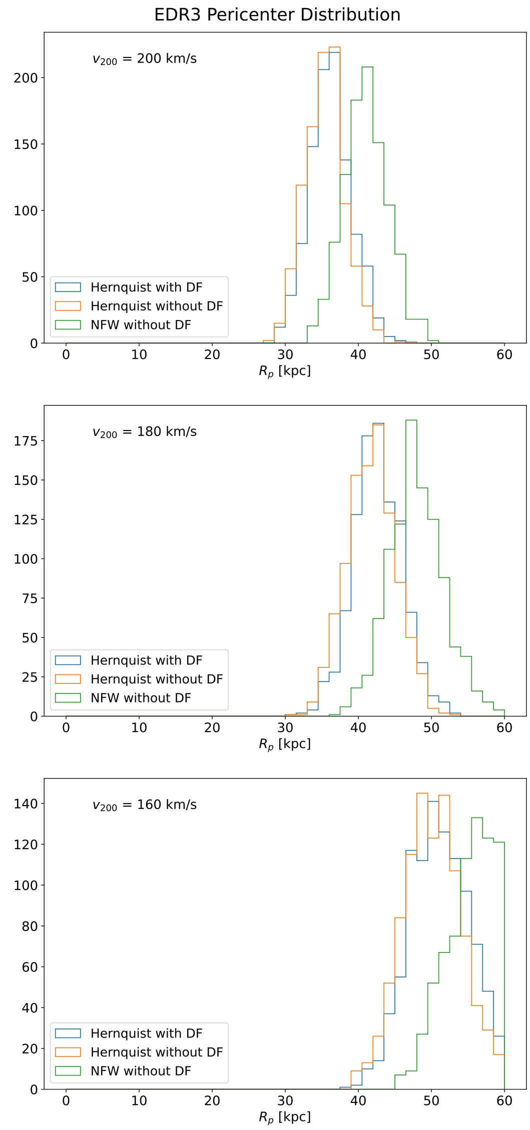

Figure 3: EDR3 pericenter distributions using 1000 samples from proper motion calculations made by McConnachie and Venn (2020) with varying virial masses. We used the same criteria as Figure 2 to integrate the orbits and plot step histograms. The relationship varying density profiles and dynamical friction are the same across both DR-2 and EDR3 data. However, the pericenter distributions calculated using EDR3 data has significantly higher mean pericenters. The EDR3 histograms are also much narrower, which is a result of better proper motion measurements allowing us to get a more accurate picture of Antlia 2's orbit.

5. Ongoing and Future Work

We are working on using our own selection criteria to independently recalculate the proper motions of Antlia 2. To filter out foreground Milky Way stars and isolate the member stars of Antlia 2, we have a number of tools at our disposal. We first choose stars that are close to the center of Antlia 2 as reported in (Torrealba et al., 2019) (α = 143.8868, δ = -36.7673) by querying 400,000 stars within 5 degrees in the *Gaia* archive. Next, we plot $\mu_\alpha cos\delta$ against μ_δ and look for a cluster with similar proper motions. Lastly, we know that the stars in Antlia 2 should be a similar age, so we plot their luminosities (G) vs effective temperature ($B_p - R_p$) on a Hertzsprung-Russell diagram and compare them to theoretical isochrones. Choi et al. (2016) created theoretical isochrones using a 1D stellar evolution model from the pre-main sequence to the end of hydrogen burning (or carbon burning for more massive stars) and recorded G, B_p, R_p, and the age of each simulated star. By selecting a specific age and plotting these theoretical isochrones on top of the HR diagram of Antlia 2 candidates, we can narrow down member stars to those that are of similar age.

To compare our methods across data sets, we first reproduce the *Gaia* query and selection from (Chakrabarti et al., 2019). We queried 400,000 stars from *Gaia* DR-2, then made the same cuts as Chakrabarti et al. (2019): stars with parallax $\pi < 0.25$, located within 1.5 degrees from the center of Antlia 2, and with proper motion magnitude under 0.8 km/s. Figure 4 plots the queried stars on a color-magnitude diagram and proper motion space. We then queried stars from EDR3 using the same criteria to produce an analogous colour magnitude and proper motion diagrams in Figure 5. The longer integration time of EDR3 allowed for the detection of fainter stars and more accurate measurements. When comparing Figures 4 and 5, the EDR3 diagrams proper motion space has darker spots within in a smaller region, indicating more stars detected and less error in their proper motions.

Next, we will use an ensemble Markov Chain Monte Carlo (MCMC) sampler emcee Foreman-Mackey et al. (2013) to independently determine the proper motion of Antlia 2. We will then explore how different selection filters affect the resulting proper motions calculation, such as varying search radius, isochrone files, and proper motion cuts.

Acknowledgements

Tetsuto Nagashima acknowledges support from Research Experience for Undergraduate program at the Institute for Astronomy, University of Hawaii-Manoa funded through NSF grant #2050710. Tetsuto Nagashima would like to thank the Institute for Astronomy for their hospitality during the course of this project. Tetsuto Nagashima would like to thank Sukanya Chakrabarti and Peter Craig of the Rochester Institute of Technology for their continued support and mentorship.

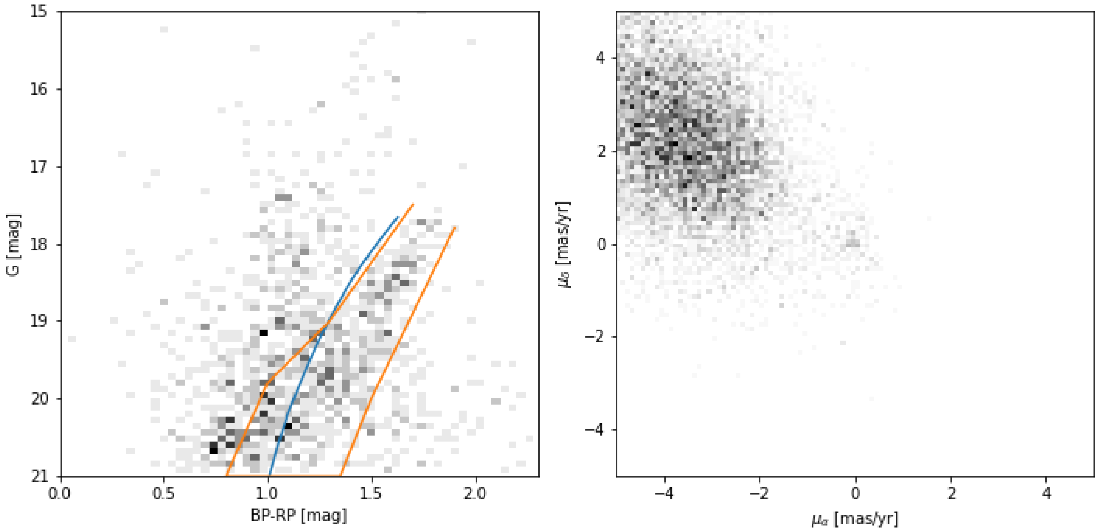

Figure 4: Reproducing Torrealba et al. (2019) CMD and proper motion graphs using Gaia DR-2. Stars were filtered by parallax $\pi < 0.25$, located within 1.5 degrees from the center of Antlia 2, and with proper motion magnitude under 0.8 km/s

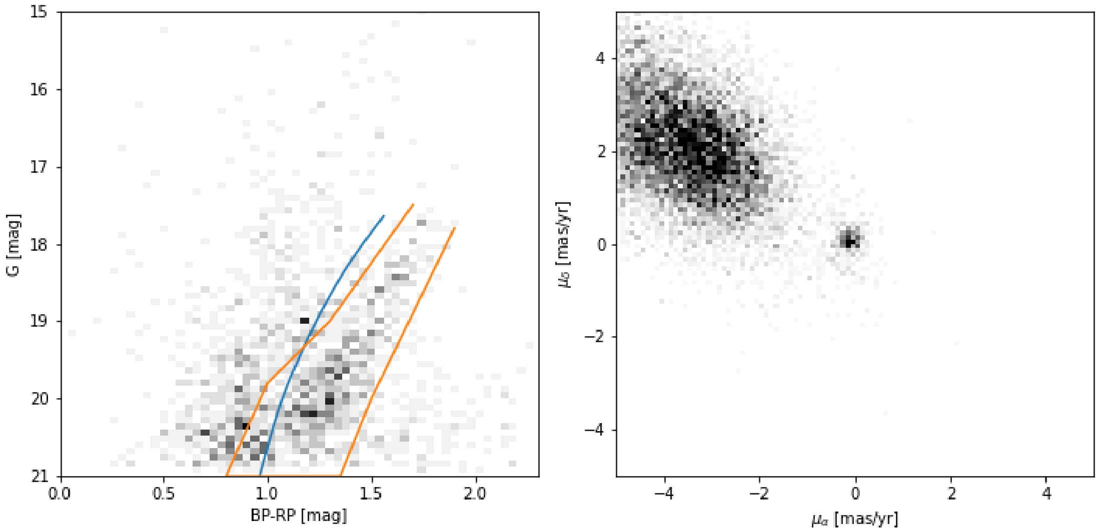

Figure 5: CMD and proper motion graphs using *Gaia* EDR3. Due to the longer integration time, EDR3 was able to detect fainter stars, which can be seen as darker spots in the proper motion histogram. A theoretical isochrone file corresponding to $[Fe/H] = -1.75$ was used to reflect the updated lower metallicity.

References

C. Auge, D. Huber, A. Heinze, B. J. Shappee, J. Tonry, S. Chakrabarti, R. E. Sanderson, L. Denneau, H. Flewelling, T. W. S. Holoien, C. S. Kochanek, G. Pignata, A. Sickafoose, B. Stalder, K. Z. Stanek, D. Stello, and T. A. Thompson. Beyond Gaia: Asteroseismic Distances of M Giants Using Ground-based Transient Surveys. AJ, 160(1):18, July 2020. doi: 10.3847/1538-3881/ab91bf.

G. Besla, N. Kallivayalil, L. Hernquist, B. Robertson, T. Cox, R. P. van der Marel, and C. Alcock. Are the magellanic clouds on their first passage about the milky way? *The Astrophysical Journal*, 668(2):949, 2007.

J. S. Bullock and K. V. Johnston. Tracing galaxy formation with stellar halos. i. methods. *The Astrophysical Journal*, 635(2):931, 2005.

S. Chakrabarti and L. Blitz. Tidal imprints of a dark subhalo on the outskirts of the milky way. *Monthly Notices of the Royal Astronomical Society: Letters*, 399(1):L118–L122, 2009.

S. Chakrabarti, P. Chang, A. M. Price-Whelan, J. Read, L. Blitz, and L. Hernquist. Antlia 2's role in driving the ripples in the outer gas disk of the galaxy. *The Astrophysical Journal*, 886(1):67, 2019.

P. Chang and S. Chakrabarti. Dark subhaloes and disturbances in extended h i discs. *Monthly Notices of the Royal Astronomical Society*, 416(1):618–628, 2011.

J. Choi, A. Dotter, C. Conroy, M. Cantiello, B. Paxton, and B. D. Johnson. Mesa isochrones and stellar tracks (mist). i. solar-scaled models. *The Astrophysical Journal*, 823(2):102, 2016.

D. Foreman-Mackey, D. W. Hogg, D. Lang, and J. Goodman. emcee: the mcmc hammer. *Publications of the Astronomical Society of the Pacific*, 125(925):306, 2013.

L. Hernquist. An analytical model for spherical galaxies and bulges. *The Astrophysical Journal*, 356:359–364, 1990.

A. P. Ji, S. E. Koposov, T. S. Li, D. Erkal, A. B. Pace, J. D. Simon, V. Belokurov, L. R. Cullinane, G. S. Da Costa, K. Kuehn, et al. Kinematics of antlia 2 and crater 2 from the southern stellar stream spectroscopic survey (s5). *arXiv preprint arXiv:2106.12656*, 2021.

E. N. Kirby, J. G. Cohen, P. Guhathakurta, L. Cheng, J. S. Bullock, and A. Gallazzi. The universal stellar mass-stellar metallicity relation for dwarf galaxies. *The Astrophysical Journal*, 779(2):102, 2013.

E. Levine, L. Blitz, and C. Heiles. The spiral structure of the outer milky way in hydrogen. *Science*, 312 (5781):1773–1777, 2006.

A. W. McConnachie and K. A. Venn. Updated proper motions for local group dwarf galaxies using gaia early data release 3. *Research Notes of the AAS*, 4(12):229, 2020.

J. F. Navarro, C. S. Frenk, and S. D. M. White. A universal density profile from hierarchical clustering. *The Astrophysical Journal*, 490(2):493–508, dec 1997. doi: 10.1086/304888. URL `https://doi.org/10.1086/304888`.

J. Read and D. Erkal. Abundance matching with the mean star formation rate: there is no missing satellites problem in the milky way above m 200 109 m. *Monthly Notices of the Royal Astronomical Society*, 487 (4):5799–5812, 2019.

V. Springel and S. D. White. Tidal tails in cold dark matter cosmologies. *Monthly Notices of the Royal Astronomical Society*, 307(1):162–178, 1999.

V. Springel, T. Di Matteo, and L. Hernquist. Modelling feedback from stars and black holes in galaxy mergers. *Monthly Notices of the Royal Astronomical Society*, 361(3):776–794, 2005.

G. Torrealba, V. Belokurov, S. Koposov, T. Li, M. Walker, J. Sanders, A. Geringer-Sameth, D. Zucker, K. Kuehn, N. Evans, et al. The hidden giant: discovery of an enormous galactic dwarf satellite in gaia dr2. *Monthly Notices of the Royal Astronomical Society*, 488(2):2743–2766, 2019.

Appendix

To develop the requisite understanding of Python, I completed a series of small projects to learn basic data analysis skills. These included plotting a circle, creating a scatterplot between two axes, a chi square goodness of fit test, creating histograms, reading and writing to a file, labeling axes, using colors, and using subplots within a plot.